

Journal of Materials Chemistry C

Low-Temperature Liquid-Crystalline Nitroxide Radical

Journal:	Journal of Materials Chemistry C
Manuscript ID	TC-ART-09-2024-004081.R1
Article Type:	Paper
Date Submitted by the Author:	13-Nov-2024
Complete List of Authors:	Uchida, Yoshiaki; Osaka University, Akita, Takuya; Osaka University, Ohkochi, Takuo; University of Hyogo; Japan Synchrotron Radiation Research Institute; RIKEN SPring-8 Center Ma, Xiao-Qian; Osaka University Kiyohara, Daichi; Osaka University Nakagami, Sho; Osaka University Yamazaki, Taira; Osaka Daigaku Nishiyama, Norikazu; Osaka University,

SCHOLARONE™ Manuscripts

ARTICLE

Low-Temperature Liquid-Crystalline Nitroxide Radical

Yoshiaki Uchida,*a Takuya Akita,a Takuo Ohkochi,b,c,d Xiao-Qian Ma,a Daichi Kiyohara,a Sho Nakagami, a Taira Yamazaki a and Norikazu Nishiyama a

Received 00th January 20xx. Accepted 00th January 20xx

DOI: 10.1039/x0xx000000x

Liquid-crystalline (LC) radicals have been considered promising as metal-free paramagnetic soft materials, but those reported so far are not easy to use because of their stability and LC temperature range. Here, we report a paramagnetic LC nitroxide radical (NR) that shows durability and tractability. The new compound shows a low melting point, high chemical stability, and high vacuum and synchrotron radiation resistance. The coexistence of the four properties enables us to take photographs of the magnetic structures of the compound on a ferromagnetic iron film using photoemission electron microscopy (PEEM). We discuss the origins of these properties. The fluorine substitution near the NR moiety significantly alters the conformational ensemble to decrease the entropy in the crystal phase. It seems beneficial to focus on conformational ensembles to incorporate bulky functional moieties into LC molecules together with durability and tractability.

Introduction

The durability of materials is critical to their development and practical uses: explosives, 1,2 hydrogen storage carriers, 3,4 liquid lithium-ion batteries,^{7–11} and conductive polymers. 12,13 Molecular materials require the realization of stabilization and high performance together because compounds with strong properties have intrinsic reactivity. Reagents with stability and reactivity are efficient for the safe production of chemicals. 14-16 Organic radicals show fascinating properties as materials, though they are generally unstable. Nitroxide radicals are relatively stable and show unique catalytic, 17 magnetic 18 and redox properties. 19

The tractability of materials at ambient temperature is also essential to be used in environments where people live. It is also true even for organic radical materials. Liquid-crystalline (LC) materials with organic stable radicals show thermal-stimuliinduced changes in magnetic properties. 20-23 Because of the air and moisture tolerance, LC nitroxide radicals (LC-NRs) could be highly promising for rapidly responsible magnetic components of mobile devices. 20,21,24,25 Their specific magnetic properties have been experimentally found and recently explained by assuming a dense network of intermolecular interactions based on molecular mobility theoretically and experimentally. 26,27 Tractable materials for applications like magnetic control of their droplets or capsules need appropriate temperature ranges in which they are stable.5 Although the LC-NRs are thermally stable up to about 150°C, the melting points that show tractable nematic (N) or chiral nematic (N*) phases are too high (>60 °C).^{28,29}

The control of phase transition temperatures of materials is of key importance for developing their functions. In most cases, mixing several LC compounds is the most conventional and simplest way to obtain ambient temperature LC materials. This method is nearly impossible without low-melting-point LC compounds like 4-cyano-4'-pentylbiphenyl (5CB),5 whose chemical stability and runny nematic (N) phase between 22 °C and 35 °C had historically made itself the gold standard molecule for LC displays and other applications.30 However, because the concentration of paramagnetic components must be kept high to form a dense network of intermolecular interactions,²⁷ the standard LC-NR is strongly required for any application. If the functional group has an appropriate shape for LC molecules, the additional function can coexist with lowmelting-point LC phases; e.g., 4-butyl-4'-methoxyazobenzene with a photoisomerizable azobenzene moiety to show photofluidization from its N phase at room temperature. 31,32

Since the rigid core generally decides the crystallinity of the LC materials, the modification of terminal units is not crucial for lowering the melting points; LC-NRs show melting points higher than 60 °C regardless of terminal units. 33–37 To lower the melting temperature $(T_f = \Delta H_f/\Delta S_f)$, we should design the compound with a lower enthalpy of fusion ($\Delta H_{\rm f}$) or a larger entropy of fusion ($\Delta S_{\rm f}$). Since the number of phenylene groups cannot be lower than three for LC-NRs not to lose the liquid crystallinity,²⁸ the chiral resolution is the only way to decrease $\Delta H_{\rm f}$. This effect is expected to be too small to lower $T_{
m f}$ to ambient temperature.²⁸ We should focus on the increase of the difference in configurational entropy between crystal and LC

^{a.} Graduate School of Engineering Science, Osaka University, 1-3 Machikaneyamacho, Toyonaka, Osaka 560-8531, Japan. E-mail: y.uchida.es@osaka-u.ac.jp

^{b.} Laboratory of Advanced Science and Technology for Industry, University of Hyogo, Kamigori, Hyogo 678-1205, Japan.

^c Japan Synchrotron Radiation Research Institute, Sayo, Hyogo 679-5198, Japan.

d. RIKEN SPring-8 Center, Sayo, Hyogo 679-5148, Japan

[†] Supplementary Information available: Synthesis methods, synthetic scheme, characterization methods, phase transition behavior, calculation results, HPLC charts, X-ray crystallographic analysis, SQUID magnetometry, EPR spectroscopy, XMCD-PEEM; Scheme S1, Figs. S1-14 and Tables S1-4. CCDC 2251603 ((2S,5S)-8FNO7). For ESI and crystallographic data in CIF or other electronic format see DOI: 10.1039/x0xx00000x

phases. The configurational entropy can be reduced in crystals even by one substitution that breaks molecular symmetry, whereas the configurational entropy in LC phases is independent of the same substitution because the molecules can rotate there.³⁸ Therefore, we anticipated that symmetry breaking by substituting any hydrogen atom in the phenylenes decreases the melting point, as shown in **Fig. 1a**. The fluorination seems appropriate due to the stability of C-F bonds and the smallest size in all possible substituents; its minimal bulkiness would hardly hinder the rod-like shape leading to the liquid crystallinity, whereas its size larger than hydrogen atom could sterically destabilize one of the conformations of the rigid groups.

Here, we describe the actual synthesis of an LC-NR showing an N* phase with a low melting point (< 40°C) by lateral fluorination (8FNO7), as shown in Fig. 1b. The molecular design process leading to this molecular structure will be unraveled in turn; three points should be noticed for energetically destabilizing crystal phases to lower melting points: fluorination, chirality and alkyl chain length. Then, we test the durability and tractability of the prepared LC-NR by detecting its magnetic structures induced by the deposited iron film using photoemission electron microscopy (PEEM) in a high vacuum under synchrotron radiation.

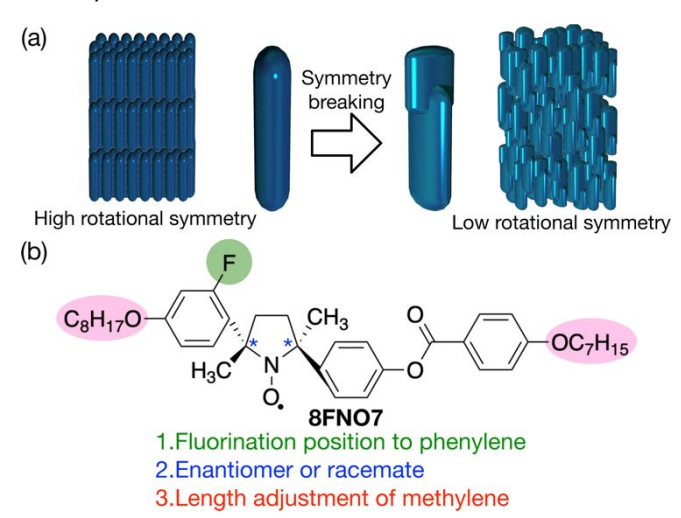


Fig. 1 Molecular design to lower the melting point for LC-NRs. (a) Strategy to lower melting points. The symmetry-breaking in molecular conformation lowers the entropy in crystals. (b) Three steps of the strategy to decrease the molecular symmetry without deteriorating liquid crystallinity: fluorination, chirality and alkyl chain length.

Results and discussion

Fluorination for decreasing entropy in crystal

To lower the configurational entropy of crystals, the rotational symmetry of the three bonds between rigid groups ($B_1 \sim B_3$ in Fig. 2a) should be broken by fluorine substituents and carbonyl or methyl groups. To inhibit the rotation around these bonds, we must consider only four fluorination positions ($X_1 \sim X_4$ positions in Fig. 2a). We synthesized fluorinated analogs, as shown in Scheme S1. The lateral fluorination at the ortho-

position of the phenoxy oxygen in a phenyl benzoate moiety typically often disrupts molecular packing in the Cr phases of calamitic LC compounds and keeps melting points low.^{39,40} We synthesized compounds laterally fluorinated at X₁ and X₂ positions. The fluorination at these positions leads to undesired results; melting points are hardly influenced by the fluorine substituents, as shown in Table S1. Moreover, the fluorination at these positions (X₁ and X₂) is likely to destabilize LC phases; the clearing points decrease about 15 $^{\circ}\text{C}$ with the fluorination at each position, and the N phases of some compounds consequently become monotropic. These results indicate that each rigid moiety in LC-NRs has a different role in deciding the phase behaviors. The phenyl benzoate group must rotate around the B₁ bond to stabilize LC phases better than isotropic phases. The bulky five-membered-ring NR moiety in the mesogen core, in which 2,5-dimethyl-2,5-diphenylpyrrolidin-1oxy (DDPO moiety) is chemically stabilized by the bulkiness, would dominate the molecular packing that decides the stability of crystalline phases.

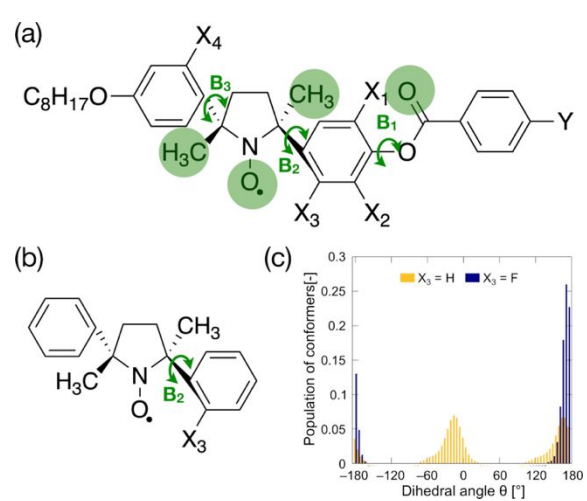


Fig. 2 The effect of the fluorination. (a) Fluorination positions: $X_1 \sim X_4$. The fluorine atoms at the X_1 and X_2 positions interfere with carbonyl oxygen and inhibit the rotation of the bond B_1 . The fluorine atoms at the X_3 and X_4 positions interfere with one of the methyl groups and nitroxyl oxygen, and they inhibit the rotation of the bonds B_2 and B_3 , respectively. Y is the alkoxy, alkyl or cyano group. (b) DDPO fluorinated at the X_3 position should show the asymmetric rotation around B_2 . (c) The dependence of population of conformers of fluorinated and non-fluorinated DDPO at the X_3 position on the dihedral angle around B_2 .

The fluorination at the X_3 and X_4 positions should inhibit the rotation of the bonds in the DDPO group. First, we examine the effect of the fluorination at the X_3 position. It tends to slightly but surely lower melting points and to maintain the stability of LC phases; the melting points of (\pm)-8NOF8 and (\pm)-8NOFC8 are 5.2 and 20.1°C lower than the corresponding non-fluorinated compounds (\pm)-8NO8 and (\pm)-8NOC8, respectively, as shown in Table S2.

To confirm the influences of fluorination at this position, the dihedral angle (N1–C6–C7–C8) and bond angle (N1–C2–C5) were calculated as a function of the dihedral angle θ (N1–C2–C3–C4) for the fluorinated (X₃ = F) and non-fluorinated (X₃ = H) DDPO shown in **Fig. 2b** at the UBLYP/6-31G** level using the Gaussian 09 program package, as shown in **Fig. S1**.⁴¹ The results

of conformational analyses by DFT calculations suggest that the fluorination drastically changes the conformational ensemble, as shown in Fig. 2c. The conformation of fluorinated DDPO (X₃ = F) is biased to $\theta = \pm 180^\circ$ so that the fluorine atom avoids getting closer to the NR oxygen. The increase of ΔS_f lowers T_f . The conformational bias is likely to give rise to the chemical stability, too. Moreover, the fluorination at the X₄ position is expected to be as effective as that at the X₃ position. The fluorination at the X₄ position does not seem effective for the racemates, as listed in Table S3. These results differ completely from those in enantiomerically enriched LC-NRs fluorinated at the X₃ and X₄ positions.

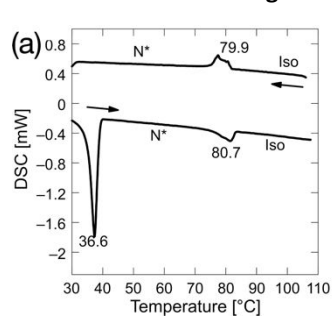
Chiral resolution for decreasing the symmetry

In the case of LC-NRs, racemates tend to constitute more stable crystal structures than the enantiomers of the same compounds. 24,35,37 It suggests that we are hopefully able to thermally destabilize the crystal structure very much. The decrease of $\Delta H_{\rm f}$ lowers $T_{\rm f}$. However, whether racemates or pure enantiomers thermally stabilize the crystal structure depends on the intermolecular arrangement of the molecules packed in the crystal. We have no choice but to try to synthesize the analogs.

We carried out the chiral resolution of racemates by high-performance liquid chromatography (HPLC) using a chiral column, as shown in **Fig. S2**. Enantiomerically enriched fluorinated compounds (2*S*,5*S*)-**8NOF8** and (2*R*,5*R*)-**8FNO8** show much lower melting points than their racemates (±)-**8NOF8** and (±)-**8FNO8**, whereas non-fluorinated (±)-**8NO8** and (2*S*,5*S*)-**8NO8** show similar melting points to each other as shown in **Table S2**.

Alkyl chain length for worse packing

To lower melting points as much as possible, we fine-tuned the length of alkoxy side chains of the enantiomerically enriched LC-NR fluorinated at the most effective position, as shown in **Table S4**. All compounds show enantiotropic N* phases and lower melting points than the corresponding racemates. Among them, (2*S*,5*S*)-8FNO7 has the lowest melting point of 36.6 °C and the widest N* phase temperature range of 43.6 °C, as shown in **Fig. 3**. The enantiomerically enriched 8FNO7 (>99% *ee*) showed a lower melting point than the samples with lower *ee*, as shown in **Fig. S3**. These results confirm that paired enantiomers would promote the molecular packing to form high melting-point racemic compound (RC) crystals. It is supported by an X-ray crystal structure of (2*S*,5*S*)-8FNO7, as shown in **Table S5** and **Fig. S4**.



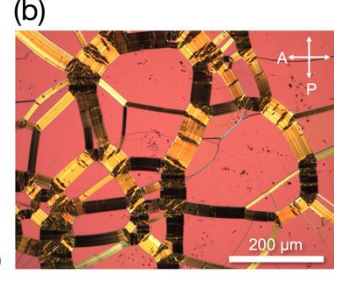


Fig. 3 Phase transition behavior of (2*S*,5*S*)-8FNO7. (a) DSC curves for (2*S*,5*S*)-8FNO7. Transition temperatures are shown with the standard notation of the phases: chiral nematic (N*) and isotropic (Iso) phases. (b) Polarized optical micrographs of (2*S*,5*S*)-8FNO7. An oily-streak texture for the N* phase at 62.0 °C. The orientations of the polarizer (P) and analyzer (A) are shown.

In addition, (25,55)-8FNO7 has high thermal stability up to 200 °C in the air, as shown in Fig. S5 and moisture tolerance. Its chemical stability, low melting point, and wide temperature range of the N* phase should be advantageous to PEEM. These results imply that the design of the LC molecule with a functional moiety should be started from the modification around the functional moiety. In addition to breaking rotational symmetry around the DDPO moiety in (25,55)-8FNO7, breaking mirror symmetry destabilizes the high melting-point RC crystalline phase.

Magnetic properties of (25,55)-8FNO7

As another requirement for PEEM combined with the X-ray magnetic circular dichroism (XMCD), we confirmed the magnetic properties of (2S,5S)-8FNO7 using superconducting quantum interference device (SQUID) magnetometry and electron paramagnetic resonance (EPR) spectroscopy, as shown in Fig. 4 and Figs. S6-S12. Crystals of (2S,5S)-8FNO7 showed weak antiferromagnetic interactions in the low-temperature range, whereas N* and isotropic (Iso) phases of (2S,5S)-8FNO7 exhibited a positive magneto-LC effect; the paramagnetic susceptibility χ_{para} distinctively increases by SQUID magnetometry with 0.05 T of the magnetic field, as shown in Fig. 4 and the relative magnetic susceptibility χ_{rel} increases by 14.7% by EPR spectroscopy with 0.33 T of the magnetic field at the Cr-to-N* phase transition (36.6 °C) in the first heating process like the non-fluorinated compound (2S,5S)-8NO8, as shown in Figs. S11. The increase in magnetic susceptibility is well-known to depend on the magnetic field. 20,21,24,26,28 These results indicate that almost all radicals are alive and they can interact with the other paramagnetic substances. The fluorination at the X₄ position near NR oxygen did not disrupt magnetic properties in the fluid phases.

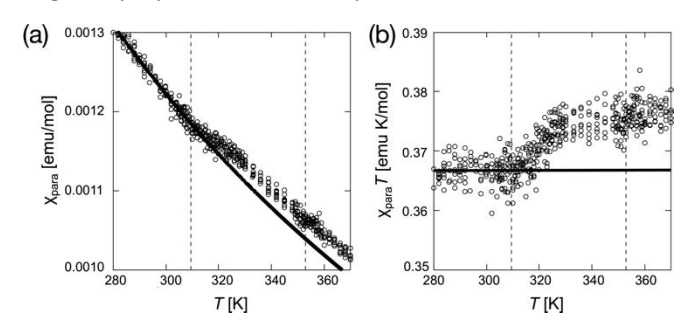


Fig. 4 The changes in magnetic properties at the phase transitions of (25,5S)-8**FNO7**. (a) χ_{para} -T plots at a magnetic field of 0.05 T. (b) χ_{para} -T plots at a magnetic field of 0.05 T. The circles denote the experimental data in the first heating run, the solid lines denote the Curie-Weiss curve fitted between 280 and 305 K, and the vertical dotted lines denote the Cr-to-N* and N*-to-Iso phase transition temperatures.

Photoemission electron microscopy (PEEM)

We can test the durability of (2*S*,5*S*)-**8FNO7** using PEEM because the sample must be put in a high vacuum under

synchrotron radiation. We measured X-ray absorption spectroscopy (XAS) using the PEEM. First, (2S,5S)-8FNO7 was spin-coated on a P-type silicon substrate. Note that poly(vinyl alcohol) (PVA) was spin-coated onto the Si substrate before applying the LC-NR because of the poor wettability of the substrate. To overcome the charging problem that may occur for insulating (2S,5S)-8FNO7 in electron imaging, we employed the method of Au pattern deposition, as schematically shown in Fig. 5a. The sample was covered by thick Au (~100 nm) except for a thin area for the observation with a 30 mm width. The XAS spectra were obtained by extracting X-ray PEEM image intensities with sweeping photon energies across the O *K*-absorption edges, as shown in Fig. 5b. It suggests that the edges originate from the LC-NR containing oxygen atoms. The LC-NR is stable in a vacuum and stable against synchrotron radiation.

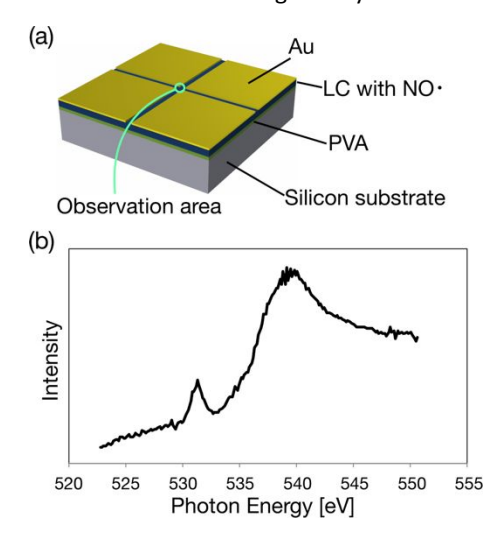


Fig. 5 Photoemission electron microscopy (PEEM). (a) Schematic illustration of the sample prepared for PEEM. PVA was spin-coated onto Si substrate before applying (25,55)-**8FNO7** and Au was coated to avoid charging. (b) X-ray absorption spectroscopy (XAS) spectrum around the O K-edge of (25,55)-**8FNO7**.

X-ray magnetic circular dichroism (XMCD)

Furthermore, XMCD-PEEM is the most powerful method for detecting magnetic structures. Although XMCD-PEEM is generally used to measure the domains of ferromagnetic materials, it can also be used to measure the magnetic structures of paramagnetic materials like oxygen atoms. Magnetic moments can be induced into oxygen atoms or carbon monoxide molecules contacting ferromagnetic metal through exchange interactions.^{43,44} We confirmed that the oxygen atoms are likely to be magnetized by the direct exchange interactions with the iron film, as shown in **Fig. S13**.

We deposited iron (2 nm) on (2*S*,5*S*)-**8FNO7** covered by thick Au except for a thin observation area of the width of 30 μ m (**Fig. 6a**). XAS spectra of the sample at the Fe L_3 -edge were drawn using the same method mentioned above (**Fig. 6b**). It means that the thin film is not iron oxide but iron metal. Then, we took XMCD-PEEM images to visualize the magnetic domains of the thin iron film, as shown in **Fig. 6c**. The XMCD-PEEM image of the Fe L_3 -edge exhibits a clear domain structure. We confirmed that the XMCD image contrast varies by changing the direction of incident X-ray beams (by rotating the sample in-plane), as

shown in Fig. S14, suggesting that the iron film has in-plane magnetization. We took the XMCD-PEEM images at the O Kedge in the same field of view (30976 pixels) for Fe L_3 -edge measurement. The XMCD-PEEM image of the O K-edge exhibits a very faint but discernible XMCD contrast indicative of the induced magnetic domain structure of (2S,5S)-8FNO7, as shown in Fig. 6d. We verified that the correlation between the XMCD contrast of the Fe L3-edge and the O K-edge almost linearly increases as we add up the number of obtained XMCD-PEEM images of the O K-edge from 10,000 to 114,000, as shown in Fig. 6e. (2S,5S)-8FNO7 was stable after the synchrotron radiation in a vacuum for one week. Although the XMCD-PEEM signal might depend on the morphology of samples, the correlation is sufficient (0.26). We can conclude that the XMCD contrast at the O K-edge derives from the magnetization induced by iron atoms.

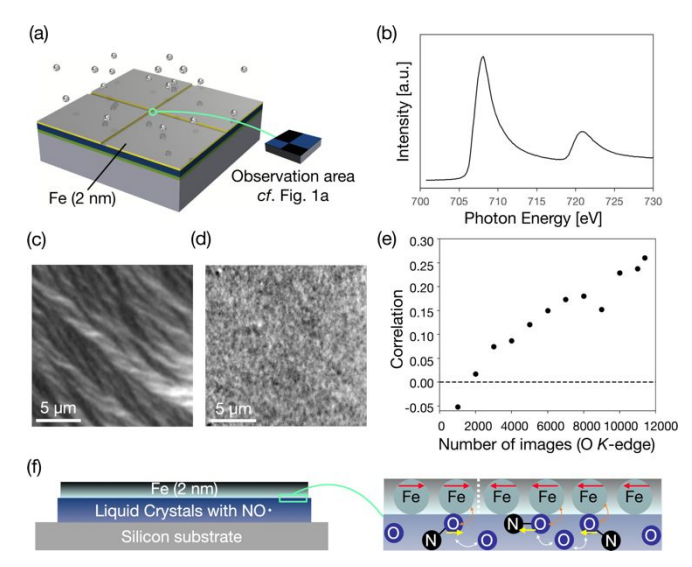


Fig. 6 XMCD-PEEM images of iron-coated (25,55)-8**FNO7**. (a) Schematic illustration of the sample prepared for XMCD-PEEM. (b) XAS spectrum around the Fe L_3 -edge of the iron film deposited on the sample. (c) XMCD-PEEM image at the absorption peak of the Fe L_3 -edge (708 eV). (d) XMCD-PEEM image of the same region of the sample as (c) at the absorption peak of the O *K*-edge (530 eV). (e) Correlation between the XMCD-PEEM images at the Fe L_3 -edge (c) and the O *K*-edge (d). It increases with the increasing number of images at the O *K*-edge. (f) Iron atoms deposited on the LC-NR interact with the oxygen atoms in the LC-NR molecules.

Experimental

General Information

Mass spectra were recorded on a JEOL JMS-700. IR spectra were recorded with a SHIMADZU IRAffinity-1 using the KBr-pellet technique. Elemental analyses (CHN) were carried out using a PerkinElmer 2400II. The g-values and hyperfine coupling constants ($a_{\rm N}$) were determined by the EPR spectra of tetrahydrofuran (THF) solutions at room temperature recorded with a JEOL JES-FE1XG in a magnetic field of about 0.33 T (X-band). Magnetization was recorded with a QUANTUM DESIGN MPMS-3. Phase behaviors were determined by differential scanning calorimetry (SHIMADZU DSC-60) and polarized optical microscopy (Olympus BX51). A hot stage (Japan High Tech

ARTICLE

10083) was used as the temperature control unit for the microscopy. The thermal stability of compounds was evaluated by thermogravimetric analysis (SHIMADZU DTG-60). Bright-field optical microscope equipped with a CMOS camera (Point Grey, FL3-U3-13S2C-CS) was used to observe the generation processes of microcapsules. Unless otherwise noted, solvents and reagents were reagent grade and used without further purification. THF that was used for chemical reactions and the EPR spectroscopy was distilled from sodium/benzophenone ketyl under nitrogen. Silicon substrates for XAS and XMCD-PEEM were p-type silicon (NILACO, Japan, resistivity $\leqq 0.02~\Omega \cdot cm^{-1}$).

Phase transition

The phase behaviors were characterized by differential scanning calorimetry (DSC) at a scanning rate of 2 °C/min upon first heating and cooling processes and by polarized optical microscopy (POM).

Conformational Analysis

We conducted conformational analyses to study shape symmetry and molecular dipole moments by DFT calculations at the UB3LYP/6-31G** level using Gaussian 09 program package. 41 The energy of each conformer of the derivatives as a substructure of the LC-NRs was calculated as a function of dihedral angle ϑ . And we also calculated the population of each conformer by assuming Boltzmann distribution at 300 K as follows.

$$\frac{N_i}{N_{\text{total}}} = \frac{e^{-\Delta E_i/RT}}{\sum_{k=1}^{N_{\text{total}}} e^{-\Delta E_k/RT}} \ . \tag{1}$$

Evaluation of Magnetic Properties by SQUID Magnetometry

In the first heating process, the temperature dependences of molar magnetic susceptibility $\chi_{\rm M}$ were measured on an MPMS superconducting quantum interference device (SQUID) magnetometer. Each 5–10 mg sample was enclosed in a DSC aluminum pan to prevent the sign inversion of the total magnetic susceptibility of samples mounted in a drinking straw in high-temperature ranges. Curie constant C and Weiss constant C were evaluated by fitting experimental magnetic susceptibility data with the following equation involving the term of Curie—Weiss law and small diamagnetic contribution $\chi_{\rm dia}$

$$\chi_{\rm M} = \frac{C}{T - \theta} + \chi_{\rm dia} \,. \tag{2}$$

Sample preparation for XAS and XMCD-PEEM

An aqueous solution (0.1 wt%) of poly(vinyl alcohol) (PVA, Mw = 1500, 86 $^{\sim}$ 89% hydrolyzed) was spin-coated at 200 rpm on the Si and ITO substrates. After drying the substrates at 180 $^{\circ}$ C for 12 h, a hexane solution (0.1 wt%) of (25,55)-8FNO7 was spin-coated at 5000 rpm on PVA. To effectively release the positive charges created by photoemission, we deposited *ex situ* thick (typically $^{\sim}$ 100 nm) Au films just around the observation area (30 mm). Then, we deposited *in situ* thin (typically $^{\sim}$ 2 nm) Fe films.

XAS and XMCD-PEEM

The experiments were performed at the PEEM experimental station of beamline BL17SU (a-branch) of SPring-8. 45,46 In this beamline, circularly or linearly polarized soft X-rays (200–2000 eV) generated from a multi-polarization-mode undulator are available. 47 Although the soft X-ray beams can be focused down to $^{\sim}15~\mu m$ by a condensing mirror, we used unfocused beam ($^{\sim}1~mm$) for this experiment to minimize irradiation damage inflicted on the organic LC-NR sample. We employed a spectroscopic photoemission/low-energy-electron microscope (SPELEEM; Elmitec Co. Ltd), achieving a spatial resolution of $^{\sim}23~nm$ even in PEEM experiments in the soft X-ray region. 48 All experiments were performed under a pressure of approximately $3-5\times10^{-9}$ torr and at room temperature.

Correlation between the XMCD-PEEM image at the Fe L_3 -edge and that at the O K-edge

We estimated the correlation between the XMCD-PEEM image with 176 * 176 (30976) pixels at the Fe L_3 -edge and that at the O K-edge by comparing the difference from the average brightness value for each pixel. Correlation (r) is calculated as

$$r = \frac{\sum_{i=1}^{n} (x_i - \overline{x}) (y_i - \overline{y})}{\sqrt{\sum_{i=1}^{n} (x_i - \overline{x})^2} \sqrt{\sum_{i=1}^{n} (y_i - \overline{y})^2}},$$
 (3)

where x_i and y_i are the brightness values for the images at the Fe L_3 -edge and the O K-edge, respectively, \overline{x} and \overline{y} are the average of the brightness values for the images at the Fe L_3 -edge and the O K-edge, respectively, and n is the number of pixels.

Conclusions

A comprehensive design strategy based on the conformational distribution lowers melting points while keeping magnetic properties. The obtained compound shows the lowest melting point (36.6 °C), the widest enantiotropic N* phase temperature range (43.6 °C), high thermal and chemical stability, and a positive magneto-LC effect. The design strategy focusing on conformational ensembles in the most influential substructure in the crystallinity would be universally applicable to organic materials. The PEEM of the new LC-NR suggests its durability in a vacuum and in synchrotron radiation. We observed XMCD-PEEM of the new material. This is the first work to visualize the magnetic structures in LC phases. Furthermore, this compound would be widely applicable as a metal-free compound for magnetically transportable carriers in optofluidics.^{49–52}

Author contributions

Y.U., T.A. and T.O. designed the study; T.A., D.K., X.-Q.M., S.N. and T.Y. performed the synthesis, the measurements and the analyses of phase behavior and magnetic properties; T.O. performed the XAS and XMCD-PEEM measurement and their analyses; Y.U., T.A., T.O. and N.N. wrote the paper. All authors discussed and commented on the paper.

Conflicts of interest

There are no conflicts to declare.

Data availability

The data supporting this article have been included as part of the Supplementary Information.

Acknowledgements

The experiments at SPring-8 were performed with the approval of the Japan Synchrotron Radiation Research Institute (Proposal 2016B1189, 2017A1220, 2017B1236, 2018A1183, 2018A1404, 2018B1096 and 2018B1075 (BL17SU)). The authors extend appreciation to Professor Tsuyoshi Kimura, the University of Tokyo, for SQUID magnetometry, to Professor Takeshi Naota and Dr. Takatoshi Maeda, Osaka University, for X-ray crystal structural analysis, to Professor Miki Hasegawa, Professor Rui Tamura and Dr. Naoto Nakano, Kyoto University, for helpful advice, and to Dr. Misaki Ota, Mr. Takeru Omiya, Mr. Takuto Nakai, Mr. Takuya Naruta, Mr. Koki Sasaki, Ms. Eriko Moriwaki, Osaka University, for XMCD-PEEM experiments. This work was supported in part by the Japan Science and Technology Agency (JST) 'Precursory Research for Embryonic Science and Technology (PRESTO)' for a project of 'Molecular technology and creation of new function,' by JSPS KAKENHI Grant Numbers JP17H04896, JP20K21226, JP20H05161 and JP22H02158, by "the Itoh Chubei Foundation," and by "Toyota Physical and Chemical Research Institute Scholars." T.A. is very grateful to the JSPS Research Fellowships for Young Scientists JP16J05585. The computations were performed using Research Center for Computational Science, Okazaki, Japan.

Notes and references

- 1 United States, US78317A, 1868.
- 2 P. Ravi, D. M. Badgujar, G. M. Gore, S. P. Tewari and A. K. Sikder, *Propellants Explos. Pyrotech.*, 2011, **36**, 393–403.
- 3 J. J. Jr. Reilly and R. H. Jr. Wiswall, *Inorg. Chem.*, 1968, **7**, 2254–2256.
- 4 C. Abetz, P. Georgopanos, C. Pistidda, T. Klassen and V. Abetz, *Adv. Mater. Technol.*, 2022, **7**, 2101584.
- G. W. Gray, K. J. Harrison and J. A. Nash, *Electron. Lett.*, 1973,9, 130.
- 6 D. Dunmur and T. Sluckin, *Soap, Science, and Flat-Screen TVs:*A History of Liquid Crystals, Oxford Univ Pr on Demand,
 Oxford, Reprint 版., 2014.
- 7 M. S. Whittingham, *Science*, 1976, **192**, 1126–1127.
- 8 A. Magasinski, P. Dixon, B. Hertzberg, A. Kvit, J. Ayala and G. Yushin, *Nat. Mater.*, 2010, **9**, 353–358.
- M. Li, J. Lu, Z. Chen and K. Amine, Adv. Mater., 2018, 30, 1800561.
- 10 J. Lopez, D. G. Mackanic, Y. Cui and Z. Bao, *Nat. Rev. Mater.*, 2019, **4**, 312–330.
- 11 J. Piątek, S. Afyon, T. M. Budnyak, S. Budnyk, M. H. Sipponen and A. Slabon, *Adv. Energy Mater.*, 2021, **11**, 2003456.

- 12 H. Shirakawa, E. J. Louis, A. G. MacDiarmid, C. K. Chiang and A. J. Heeger, J. Chem. Soc., Chem. Commun., 1977, 578–580.
- 13 S. C. Rasmussen, ChemPlusChem, 2020, 85, 1412-1429.
- 14 P. T. Nyffeler, S. G. Durón, M. D. Burkart, S. P. Vincent and C.-H. Wong, *Angew. Chem. Int. Ed.*, 2005, **44**, 192–212.
- 15 B. Gutmann, D. Cantillo and C. O. Kappe, *Angew. Chem. Int. Ed.*, 2015, **54**, 6688–6728.
- 16 O. O. Grygorenko, D. M. Volochnyuk and B. V. Vashchenko, Eur. J. Org. Chem., 2021, 2021, 6478–6510.
- 17 T. Saito, Y. Nishiyama, J.-L. Putaux, M. Vignon and A. Isogai, *Biomacromolecules*, 2006, **7**, 1687–1691.
- 18 M. W. Dale and C. J. Wedge, Chem. Commun., 2016, 52, 13221–13224.
- 19 B. Liu, C. W. Tang, H. Jiang, G. Jia and T. Zhao, *ACS Sustainable Chem. Eng.*, 2021, **9**, 6258–6265.
- 20 Y. Uchida, N. Ikuma, R. Tamura, S. Shimono, Y. Noda, J. Yamauchi, Y. Aoki and H. Nohira, *J. Mater. Chem.*, 2008, **18**, 2950–2952.
- 21 Y. Uchida, K. Suzuki, R. Tamura, N. Ikuma, S. Shimono, Y. Noda and J. Yamauchi, *J. Am. Chem. Soc.*, 2010, **132**, 9746–9752.
- 22 P. Ravat, T. Marszalek, W. Pisula, K. Müllen and M. Baumgarten, *J. Am. Chem. Soc.*, 2014, **136**, 12860–12863.
- 23 S. Kapuściński, J. Szczytko, D. Pociecha, M. Jasiński and P. Kaszyński, *Mater. Chem. Front.*, 2021, **5**, 6512–6521.
- 24 K. Suzuki, Y. Uchida, R. Tamura, S. Shimono and J. Yamauchi, *J. Mater. Chem.*, 2012, **22**, 6799–6806.
- 25 Y. Uchida, T. Sakaguchi, S. Oki, S. Shimono, J. Park, M. Sugiyama, S. Sato, E. Zaytseva, D. G. Mazhukin and R. Tamura, *ChemPlusChem*, 2022, **87**, e202100352.
- 26 S. Nakagami, T. Akita, D. Kiyohara, Y. Uchida, R. Tamura and N. Nishiyama, *J. Phys. Chem. B*, 2018, **122**, 7409–7415.
- 27 Y. Uchida, G. Watanabe, T. Akita and N. Nishiyama, *J. Phys. Chem. B*, 2020, **124**, 6175–6180.
- 28 N. Ikuma, R. Tamura, S. Shimono, N. Kawame, O. Tamada, N. Sakai, J. Yamauchi and Y. Yamamoto, *Angew. Chem. Int. Ed.*, 2004, **43**, 3677–3682.
- 29 R. Tamura, Y. Uchida and K. Nagura, in *Nitroxides*, eds. O. Ouari and D. Gigmes, Royal Society of Chemistry, Cambridge, 2021, pp. 420–448.
- 30 H. Kawamoto, in 2012 Third IEEE HISTory of Electrotechnology CONference (HISTELCON), 2012, pp. 1–6.
- 31 T. Ikeda and O. Tsutsumi, Science, 1995, 268, 1873-1875.
- 32 T. Ikeda, J. Mater. Chem., 2003, 13, 2037-2057.
- 33 T. Akita, T. Yamazaki, Y. Uchida and N. Nishiyama, Polyhedron, 2017, 136, 79–86.
- 34 T. Akita, Y. Uchida and N. Nishiyama, *Chem. Lett.*, 2016, **45**, 910–912.
- 35 T. Akita, Y. Uchida, D. Kiyohara, S. Nakagami and N. Nishiyama, *Ferroelectrics*, 2016, **495**, 97–104.
- 36 T. Akita, Y. Uchida and N. Nishiyama, *Mol. Cryst. Liq. Cryst.*, 2015, **613**, 174–180.
- 37 T. Akita, D. Kiyohara, T. Yamazaki, Y. Uchida and N. Nishiyama, J. Mater. Chem. C, 2017, 5, 12457–12465.
- 38 R. Pinal, Org. Biomol. Chem., 2004, 2, 2692–2699.
- 39 J. W. Goodby, E. J. Davis, R. J. Mandle and S. J. Cowling, in *Handbook of Liquid Crystals*, John Wiley & Sons, Ltd, 2014, pp. 1–30.
- 40 M. J. S. Dewar and A. C. Griffin, *J. Am. Chem. Soc.*, 1975, **97**, 6662–6666.
- 41 M. J. Frisch, G. W. Trucks, H. B. Schlegel, G. E. Scuseria, M. A. Robb, J. R. Cheeseman, G. Scalmani, V. Barone, B. Mennucci,

Journal of Materials Chemistry C

- G. A. Petersson, H. Nakatsuji, M. Caricato, X. Li, H. P. Hratchian, A. F. Izmaylov, J. Bloino, G. Zheng, J. L. Sonnenberg, M. Hada, M. Ehara, K. Toyota, R. Fukuda, J. Hasegawa, M. Ishida, T. Nakajima, Y. Honda, O. Kitao, H. Nakai, T. Vreven, J. A. Montgomery, J. E. Peralta, F. Ogliaro, M. Bearpark, J. J. Heyd, E. Brothers, K. N. Kudin, V. N. Staroverov, R. Kobayashi, J. Normand, K. Raghavachari, P. G. Rendell, J. C. Burant, S. S. Iyengar, J. Tomasi, M. Cossi, N. Rega, J. M. Millam, M. Klene, J. E. Knox, J. B. Cross, V. Bakken, C. Adamo, J. Jaramillo, R. Gomperts, R. E. Stratmann, O. Yazyev, A. J. Austin, R. Cammi, C. Pomelli, J. W. Ochterski, R. L. Martin, K. Morokuma, V. G. Zakrzewski, G. A. Voth, P. Salvador, J. J. Dannenberg, S. Dapprich, A. D. Daniels, O. Farkas, J. B. Foresman, J. V. Ortiz, J. Cioslowski, and D. J. Fox, Gaussian 09 Revision D.01, Gaussian, Inc., Wallingford CT, 2009.
- 42 T. Ohkochi, M. Kotsugi, K. Yamada, K. Kawano, K. Horiba, F. Kitajima, M. Oura, S. Shiraki, T. Hitosugi, M. Oshima, T. Ono, T. Kinoshita, T. Muro and Y. Watanabe, *J. Synchrotron. Rad.*, 2013, **20**, 620–625.
- 43 C. Sorg, N. Ponpandian, M. Bernien, K. Baberschke, H. Wende and R. Q. Wu, *Phys. Rev. B*, 2006, **73**, 064409.
- 44 K. Amemiya, T. Yokoyama, Y. Yonamoto, M. Miyachi, Y. Kitajima and T. Ohta, *Jpn. J. Appl. Phys.*, 2000, **39**, L63.
- 45 H. Ohashi, Y. Senba, H. Kishimoto, T. Miura, E. Ishiguro, T. Takeuchi, M. Oura, K. Shirasawa, T. Tanaka, M. Takeuchi, K. Takeshita, S. Goto, S. Takahashi, H. Aoyagi, M. Sano, Y. Furukawa, T. Ohata, T. Matsushita, Y. Ishizawa, S. Taniguchi, Y. Asano, Y. Harada, T. Tokushima, K. Horiba, H. Kitamura, T. Ishikawa and S. Shin, *AIP Conf. Proc.*, 2007, **879**, 523–526.
- 46 Y. Senba, H. Ohashi, H. Kishimoto, T. Miura, S. Goto, S. Shin, T. Shintake and T. Ishikawa, *AIP Conf. Proc.*, 2007, **879**, 718–721.
- 47 K. Shirasawa, T. Tanaka, T. Seike, A. Hiraya and H. Kitamura, *AIP Conf. Proc.*, 2004, **705**, 203–206.
- 48 F. Z. Guo, T. Muro, T. Matsushita, T. Wakita, H. Ohashi, Y. Senba, T. Kinoshita, K. Kobayashi, Y. Saitoh, T. Koshikawa, T. Yasue, M. Oura, T. Takeuchi and S. Shin, *Rev. Sci. Instrum.*, 2007, **78**, 066107.
- 49 J. S. Sander, R. M. Erb, C. Denier and A. R. Studart, *Adv. Mater.*, 2012, **24**, 2582–2587.
- 50 Y. Uchida, Y. Iwai, T. Akita, T. Mitome, K. Suzuki, R. Tamura and N. Nishiyama, *J. Mater. Chem. B*, 2014, **2**, 4130–4133.
- 51 L.-J. Chen, L.-L. Gong, Y.-L. Lin, X.-Y. Jin, H.-Y. Li, S.-S. Li, K.-J. Che, Z.-P. Cai and C. J. Yang, *Lab Chip*, 2016, **16**, 1206–1213.
- 52 A. S. Utada, E. Lorenceau, D. R. Link, P. D. Kaplan, H. A. Stone and D. A. Weitz, *Science*, 2005, **308**, 537–541.

Data availability
The data supporting this article have been included as part of the Supplementary Information.